Title: The Global Frequency of Supershear Earthquakes

Authors: Han Bao[1], Liuwei Xu[1], Lingsen Meng[1]*, Jean-Paul Ampuero[2]

Affiliations:

[1]Earth, Planetary, Space Science, University of California, Los Angeles; CA, USA

[2]Université Côte d'Azur, IRD, CNRS, Observatoire de la Côte d'Azur; Valbonne, France

*Corresponding author. Email: meng@epss.ucla.edu

Abstract: Supershear earthquakes, whose ruptures are faster than seismic S-waves, are rare but of broad interest because they could produce destructive ground shaking and their occurrence could hold important clues about fault mechanics. Previously, only a few cases of supershear earthquakes have been reported, most of which are continental events. Here we perform a systematic global search for supershear earthquakes and report four previously undocumented oceanic supershear earthquakes, based on rupture speeds determined by Slowness-Enhanced Back-Projection and far-field Rayleigh Mach wave identification. Among all large earthquake ruptures since 2000, we find that oceanic supershear earthquakes are as frequent as continental ones, and that at least 14.0% of Mw $\geq$ 6.7 shallow strike-slip earthquakes are supershear. We observe a wider range of stable supershear rupture speeds than predicted by 2D fracture mechanics theory, possibly explained by the presence of fault damage zones or by slip obliqueness. We attribute our findings to larger seismogenic width, bimaterial effect of oceanic-continental boundaries, and dynamic weakening mechanisms that promote both supershear transitions and propagation.

Main Text:

Introduction

Supershear earthquakes, i.e. earthquakes with rupture speeds exceeding the shear wave speed, first predicted by theory and simulations (*1,2*), have been convincingly reported for only eleven shallow strike-slip earthquakes, including the 2001 Mw 7.8 Kunlun and the 2018 Mw 7.5 Palu earthquake (*3,4*) (see Table S1 for a comprehensive referenced list of previously studied supershear earthquakes, including additional events for which published results disagree). In addition to these shallow events, only one deep supershear earthquake has been reported (*5*). Rupture speed is one of the main source properties that control the impact of an earthquake: faster ruptures can generate stronger ground motions (*6,7*), if the effect is not diminished by source complexities and path effects (*8,9*). The scarcity of observed supershear ruptures hinders systematic analysis of their mechanisms, while leaving the appearance that they are rare in nature and even rarer beneath the ocean (*10-12*). More specifically, the lack of statistical analysis makes it difficult to validate theoretical findings and to address questions such as: Do structural features control the occurrence of supershear ruptures? For instance, do they happen more often on faults with wider seismogenic widths? Do they have a preferred propagation direction due to bimaterial effects? Can they propagate at sub-Eshelby speeds (slower than $\sqrt{2}$ times S-wave speed)? To investigate these questions, here we performed a systematic global search for supershear earthquakes.

A comprehensive survey of supershear earthquakes requires robust estimates of rupture speed, enabled here by combining recent advances in seismological analysis methods. Studies based on directivity effects (*13*) and teleseismic source inversions (*14*) are challenged by the trade-off between source size and rupture speed (*15*), the usage of relative low-frequency (< 0.1 Hz) contents and smoothing constraints (16). Those based on near-field recordings, such as array techniques (*17*) and early S-arrival identification (*18,19*), are limited by the scarcity of such data. On the other hand, teleseismic or regional back-projection (BP) rupture imaging (*20*) has the potential to constrain the rupture speed of large earthquakes globally, especially if travel time errors due to 3D path effects (*21*) are mitigated by the recently developed Slowness-Enhanced Back-Projection (SEBP) (*4*). This method reduces spatial biases by calibrating the path effect using recordings of nearby events (M 4-6) that have been accurately located. Because the location uncertainties of regular catalogs of oceanic earthquakes tend to be large, here we performed teleseismic double-difference relocations (*22*) to calibrate SEBP. Moreover, to properly identify imaging artifacts and quantify the uncertainties of rupture speed estimates, we conducted a comprehensive series of BP synthetic tests considering various rupture scenarios, realistic source-receiver geometry, slip distributions, waveform complexities, fault geometries, and BP parameterizations (see Method and Section 3 in Supplementary Material for details). We found that tracking the leading BP radiators significantly reduces the "shadowing" and "tailing" artifacts that distort the rupture speed estimates (Fig. S15) and that SEBP consistently underestimates rupture speed by 5% ~ 15% (see section 2 of Methods and Fig. S17), due to the averaging effect of direct and coda waves (Fig. S19 & Fig. S20). Therefore, the rupture speed inferred from SEBP is a conservative indicator of supershear ruptures. We independently validated supershear rupture speeds by identifying Rayleigh Mach waves (*23*), a unique feature of supershear earthquakes (see Methods). Using SEBP, enhanced with relocated catalogs and comprehensive uncertainty analyses, and Mach wave identification, we searched for supershear earthquakes globally by analyzing all shallow strike-slip earthquakes (depth ≤ 50 km, dip angles ≥ 70° for both nodal planes) with magnitude (Mw) ≥ 6.7 that occurred from Jan 1st, 2000 to Feb 1st, 2020, selected based on the International Seismological Center (ISC) focal mechanism bulletin (see Table S2 for selected events, see Text S1 for detailed event selection criteria). The magnitude threshold is based on the minimum resolvable rupture length for which rupture speeds can be reliably estimated (see Text S1 and Figure S21). To be eligible for the BP analysis, we require a candidate event to be recorded by at least 50% of the stations in one of the four regional arrays in continental United States (US), Alaska (AK), pan-Europe (EU), and Australia (AU) (Fig. S2).

Results

Our analysis identifies new cases of supershear earthquakes, while confirming previously reported ones. We identified 12 large-scale supershear earthquakes (rupture length ≥ 50 km) including four previously unreported earthquakes (the 2009/2018 Caribbean, 2010 Papua, and 2013 South Sandwich Island events) and confirming three recently reported supershear earthquakes (2016 Romanche (*24*), 2017 Komandorski (*25*), and 2020 Caribbean events (*26*)) (Fig. 2). Compared to these three cited studies, estimates of rupture speeds presented here should be more accurate owing to our earthquake relocations and slowness calibrations, and more objective thanks to our systematic uncertainty analysis. An additional event is labeled here as an uncertain supershear earthquake: SEBP detects supershear speeds in the 2004 Queen Charlotte earthquake, but its supershear speed can not be validated by the Mach-wave, since the pattern of highest CC values at the two sides of the frontal direction is not observed (Figure S27), likely due to its insufficiently long supershear rupture propagation (*23*) (~ 40 km). Five events show clearly an initial subshear rupture segment followed by a supershear segment. The rupture speeds of the newly detected supershear events range from moderately faster (1.1 Vs ~ 1.4 Vs), to significantly faster (1.4 Vs ~ 1.7 Vs) than the local shear wave speed (Vs). All of the newly identified supershear ruptures are beneath the ocean (Fig.3 & Table S5).

One set of supershear earthquakes studied here highlights that some fault systems are particularly prone to host supershear earthquakes. Three supershear earthquakes (including two previously unreported) occurred beneath the Caribbean Sea within 11 years, on the transform boundary between the North America and Caribbean plates (Fig. 2). The 28 May 2009 Mw 7.3 and the 10 Jan 2018 Mw 7.5 events, ruptured two segments of the submarine Swan Island Fault, west of the Mid-Cayman spreading center. The 28 Jan 2020 Mw 7.7 earthquake ruptured a segment of the Oriente Fault, east of the Mid-Cayman spreading center. The plate motion at the boundary between the North America and Caribbean plates is estimated to be ~ 19 mm/yr along this segment (*27*). As revealed by SEBP and Rayleigh Mach waves, all three events are supershear ruptures propagating predominantly towards southwest-west (Fig. 2~4). We identified two episodes of supershear ruptures in the 2009 earthquake. The first episode propagated for 100 km at 5.5 ~ 6.3 km/s. The speed uncertainty of the second 130-km-long segment is large (3.8 ~ 5.4 km/s) due to strong shadowing artifacts around 25 ~ 50 s (Fig. 3 & S4) likely caused by abrupt changes in rupture speed and/or slip distribution (Text S2, Fig. S13 & S15). The overall rupture speed is 3.2 ~ 3.8 km/s, which is similar to that reported by Graham et al. (*28*), 2.8 ~ 4.0 km/s, based on teleseismic finite fault inversion (FFI). For the 2018 earthquake, mutually consistent BPs of multiple arrays show a 150-km-long supershear propagation at 4.5 ~ 5.5 km/s (Fig. S6). The 2020 event is bilateral, though the eastward branch was significantly shorter than the westward one (Fig. S9). The westward branch initially propagated for ~80 km at a sub-Rayleigh speed of 2.2 ~ 2.6 km/s and then for ~170 km at a supershear speed of 4.6 ~ 5.6 km/s. This is resolved by both Alaska and European arrays (Fig. S7). Moreover, ground motion data of two near-fault stations, FSCY and LCCY, shows that the fault-normal particle velocity dominates that of the fault-parallel component (Fig. S30), which is a distinctive signature of supershear ruptures (*29*). Our result differs from the first report of the 2020 event based on teleseismic FFI, which shows supershear rupture speed >5 km/s both from 0 to 20 s and from 25 to 40 s after the rupture initiation (*26*). Geodetic and historical records suggest that similar-sized earthquakes in this region have a short recurrence interval of 40 ~ 50 yr (*27*). This supershear sequence underlines that for large-scale mature transform faults along plate boundaries, potential hazards of repeating supershear earthquakes and their associated strong shaking should be of great concern. A similar situation with multiple supershear events on one transform plate boundary is the Queen Charlotte Island supershear sequence: the 2013 Craig earthquake (*30*) and the 28 June 2004 Mw 6.8 event located just 50 km in the south (Fig. 3 & S5).

The two other newly-identified supershear earthquakes also occurred in oceanic transform faults. The 2010 Mw 7.0 Papua earthquake occurred on an unidentified fault west of the boundary between the Birds Head and Maoke microplates, which accommodates ~ 80 mm/yr of left-lateral motions (*31*). The rupture broke a 100-km-long segment with an overall rupture speed of 5.0 ~ 6.1 km/s (Fig. 2~4). The 2013 Mw 7.3 South

Sandwich Island earthquake occurred on an east-striking fault, as a result of the fast motion of 14 mm/yr between the South America and Antarctica plates where two large events (M 7.4 in 2006 and M 7.5 in 1973) occurred in the past 50 years (*31*). The rupture rapidly accelerated to a supershear speed of 4.9 ~ 6.2 km/s after 20 seconds and propagated for ~ 100 km (Fig. 2~4).

For previously reported supershear events, our analyses bring either confirmation or further insights on their rupture pattern. In the 2016 Mw 7.1 earthquake that struck the eastern end of the Romanche oceanic transform fault, we identified a westward back-propagating supershear rupture after an initial sub-Rayleigh eastward rupture (Fig. 2~4). This complex rupture pattern is consistent with the one reported in the first study of this event (*24*). The 17 July 2017 Mw 7.7 Komandorski earthquake occurred inside the back-arc basin of the westernmost Aleutian Islands, along a 400-km-long segment of the Bering Fracture Zone (BFZ). The BFZ accommodates approximately two thirds (5.1 cm/yr) of the relative shearing motion between the Pacific and North American plates (7.8 cm/yr), creating a prime tectonic environment for large strike-slip events (*32*). The spatiotemporal characteristics of the rupture process are well imaged by SEBP (Fig. 2). The coherent high-frequency sources follow an overall linear rupture path towards Southeast in two episodes: initial sub-Rayleigh propagation along 50 km in the first 25 s, followed by fast supershear propagation at 4.5 ~ 4.9 km/s over 200 km (Fig. 3~4). Our result differs from the first report of this event (*25*), which showed a later and much shorter supershear segment only 50 km long.

Discussion

Our results indicate that supershear earthquakes are more common than previously thought, especially owing to newly found cases in oceanic environments. Previous studies have argued that supershear earthquakes are rare (*10-12*). Indeed, before the year 2020, only five earthquakes that occurred after 2000 had been identified as shallow supershear events, rendering a rate of 5.8% among large (M ≥ 6.7) strike-slip earthquakes (Table S2). Such paucity has been attributed to insufficient prestress (*11*) or complex fault geometry (*12*), and could also be favored by off-fault dissipation mechanisms (*33*). Our analysis results in a rate of supershear events at least twice as high as the previous estimate: we find that between 2000 and 2020, 12 out of 86 large (M ≥ 6.7) shallow strike-slip earthquakes were supershear, yielding a rate of 14.0%. This is a conservative estimate not accounting for uncertain supershear events (see Table S3 for full statistics). All newly reported events are oceanic supershear earthquakes (OSEs), which were previously missed possibly due to (1) lack of near-field seismic data, (2) lack of effective approaches to detect supershear rupture with teleseismic data, and (3) less public and scientific attention because of their large distance to population centers and low casualties. The newly detected OSEs demonstrate the effectiveness of SEBP and Mach wave methods in identifying supershear ruptures at teleseismic distances. Previous observations suggested that OSEs are even rarer than their continental counterparts (*10*). However, we show that the probability of OSE is 14.3%, almost the same as that of continental supershear earthquakes (CSE), 13.5%. Because the identification by BP of a transition from subshear to supershear rupture requires a sustained supershear propagation longer than 50 km, as suggested by synthetic tests (Figure S21), the real supershear rate might be higher than our conservative estimates.

Our observations motivate the question of what controls the rate of supershear. A number of physical mechanisms might be responsible for initiating supershear ruptures. For instance, in the Burridge-Andrews model (*1,2,34*), a daughter-crack emerges ahead of the sub-Rayleigh front when the dynamic fault shear stresses between P and S waves exceed the fault strength. Other processes can facilitate supershear transition without necessarily forming daughter-cracks, including dynamic stress perturbation due to stress and strength heterogeneity (*35,36*), non-planar fault geometry (roughness/curvature/bending) (*37*), fault step-over (*38*), slip obliqueness on long strike-slip faults (*39*), interactions of rupture fronts with the free surface (*40*) and fault damage zones (*41*). Our newly estimated supershear rate of 14.0% can be compared with the supershear rate predicted in future studies by one or a combination of these mechanisms.

For some supershear mechanisms, we can identify which observable factors could in principle explain why the supershear rate is low in nature. Both in Burridge-Andrews (*1,2,33*) and Weng-Ampuero (*39, 42*) theories, supershear rupture requires sufficiently high fault stress, manifested by low ratios of strength excess to stress drop and low ratios of fracture energy Gc to strain energy release rate G0, respectively. During the interseismic period, as fault stress builds up, the possibility of supershear rupture increases with time. But if nucleation happens often, large earthquakes are likely to start before the fault reaches a stress allowing supershear rupture. The rate of supershear events thus depends on a trade-off between stressing rate and nucleation rate. The former is controlled by the ratio between the long-term fault slip rate and the seismogenic width, the latter by the background seismicity rate of the fault. Studies based on observed seismicity rates and fault loading rate may provide further insights.

Our observations show evidence of bimaterial fault effects on the prevalence and rupture direction of supershear earthquakes. Slip along bimaterial faults (separating rocks with different elastic properties) produces normal stress changes, which favors rupture propagation in a certain direction (*43*), such that supershear ruptures tend to propagate in the direction of the displacement of the stiffer side of the fault (the 'negative direction') (*44,45*). Recent bimaterial-interface experiments resolving the real contact area found that, at supershear rupture speeds, the dynamic reduction of contact area due to the coupling effect of slip and normal stress was a dominant source of weakening (*46*). To investigate bimaterial effects in supershear ruptures, we classified shallow strike-slip events into three groups: continental-continental boundary (CCB), oceanic-oceanic boundary (OOB) and oceanic-continental boundary (OCB) events. Material contrasts are expected more systematically across OCB faults, with the continental side being more compliant than the oceanic side. The supershear rates (Table S3) are much larger for OCB events (83.3%) than for CCB (13.5%) and OOB events (4.7%). Thus, the dynamic weakening due to bimaterial contrast may contribute to the sustainability of OCB supershear ruptures. In addition, our result is consistent with the preferred supershear rupture direction along bimaterial interfaces: five out of the six OCB supershear earthquakes ruptured in the 'negative' direction, the exception being the 2020 Caribbean event.

We also find evidence that larger seismogenic widths and greater fault maturity promote the sustainability of supershear ruptures. Recent theoretical studies of elongated ruptures show that the energy ratio Gc/Go on vertically-bounded faults, which controls their rupture speed, is inversely proportional to the seismogenic width (*39,42*). For shallow strike-slip events the seismogenic depth is limited by the crustal thickness, which is correlated with the plate thicknesses above Moho and above the lithosphere-asthenosphere boundary (LAB) (Table S4). According to the World's Ocean Crust Model, the average thickness above LAB of the OSE source regions is 91 km, substantially thicker than that of the non-supershear events (65 km). The average thickness above Moho of the supershear-rich regions (the Caribbean Sea and the Queen Charlotte islands) is 17.6 km, thicker than that of the non-supershear regions (11.2 km). These statistics indicate the seismogenic zones of all identified supershear earthquakes are wider, which is consistent with lower energy ratios and faster ruptures (*42*). Moreover, the supershear-rich faults tend to have tectonic slip rates larger than 1.9 cm/yr, lengths exceeding 800 km and relatively straight geometries (*27,30,32*), which suggests that these conditions are favorable for supershear propagation (*39,47*). Faults without these conditions, such as the slow and poorly developed fault hosting the 2010 Papua event and the geometrically complex fault hosting the 2018 Palu event (*4*), still produce supershear ruptures, although globally more rarely.

Our observations also provide robust evidence of supershear ruptures with rather unexpected speeds. Theories of fracture mechanics in 2D predict the stable range of supershear rupture speed is between the Eshelby speed (~ √2Vs=1.41Vs) and Vp (*1,48*). However, our results indicate supershear rupture speeds as slow as 1.15 Vs compared to a reference Vs at 10 km depth, or 1.11 Vs compared to a reference Vs at GCMT centroid depths, according to the CRUST1.0 model (Table S5). In particular, the 2017 Komandorski event ruptured along 200 km at a speed of 1.11 Vs ~ 1.21 Vs, significantly below the Eshelby speed (even after accounting for BP uncertainties, and confirmed by the Rayleigh-Mach-wave approach; see Methods). Such "slow" stable supershear ruptures may result from reduced wave speeds at shallow depth (*40*) (slip was concentrated in the upper 15 km (*49*)) or in the fault damage zone (*4,41,50*), or from slip obliqueness (*42*) (rake of 18° reported for the Komandorski event).

Figures

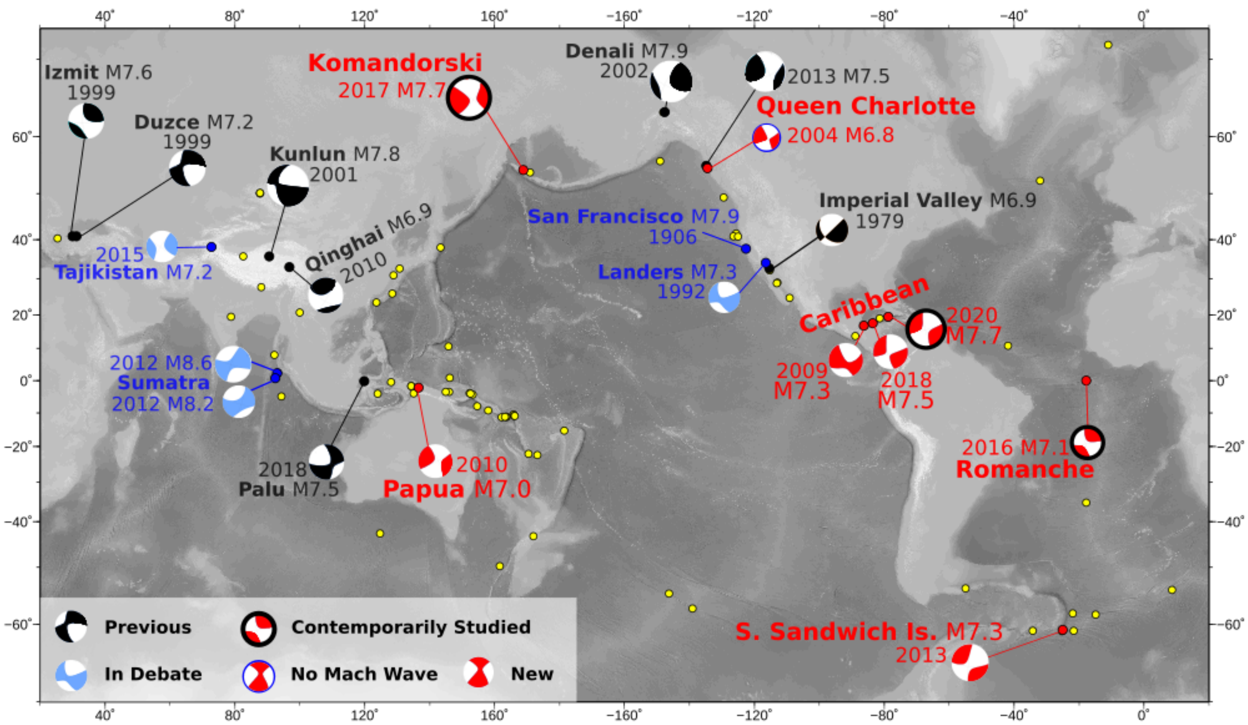

Figure 1. Global supershear earthquakes. Eight previously reported shallow strike-slip supershear earthquakes (black circles); five previously reported supershear earthquakes with debated evidence (light blue circles); four newly identified supershear earthquakes based on SEBP with evidence of Mach cones (red circles without edges); three supershear earthquakes recently studied by other groups (red circles with black edge); and one earthquake with a supershear rupture speed estimated from SEPB but without identified Mach waves (red circles with blue edge). All other examined large (M ≥ 6.7) shallow strike-slip events without resolvable supershear ruptures are marked by yellow dots.

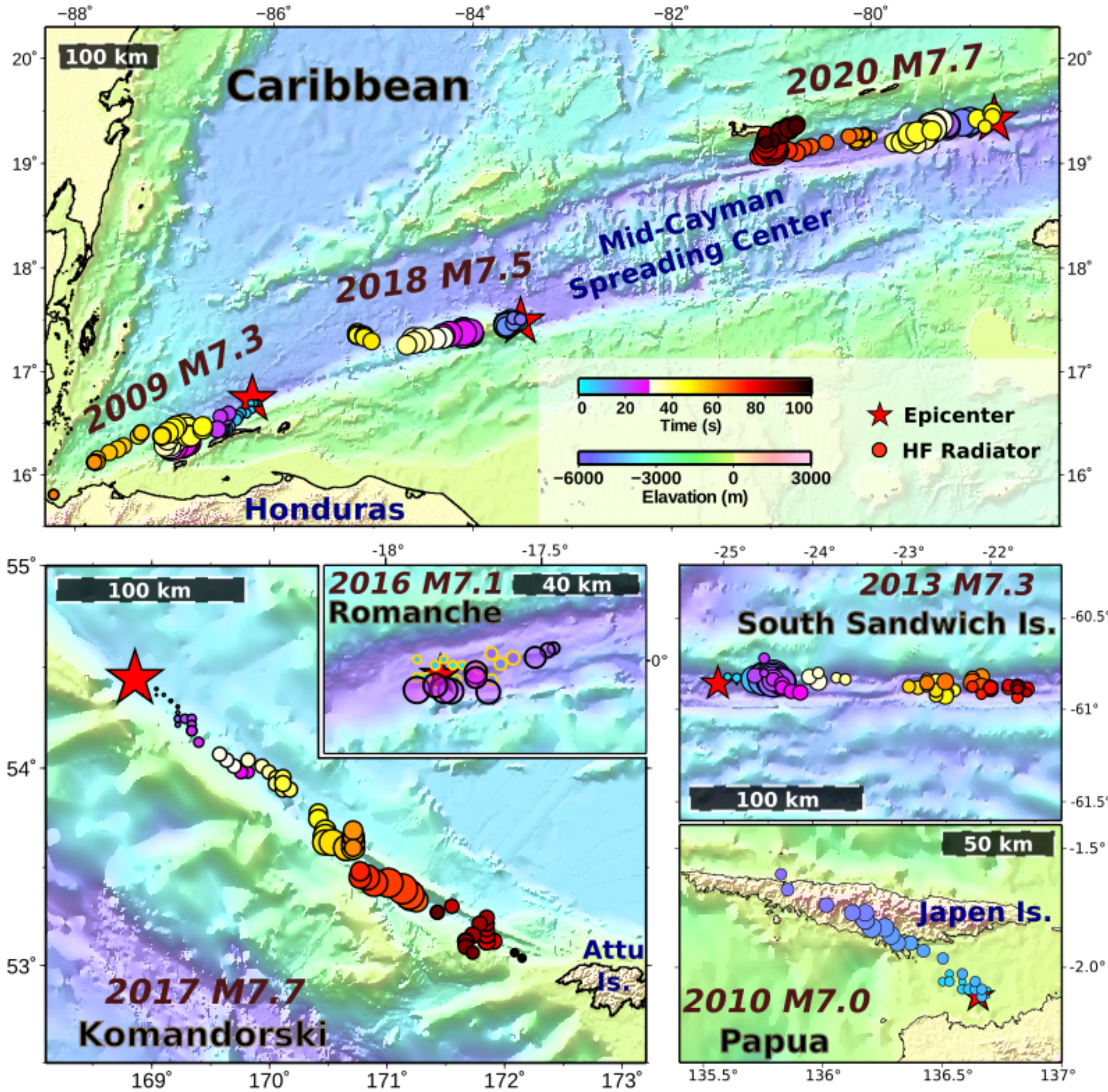

Figure 2. **Spatiotemporal distribution of high-frequency (HF) (0.5-2 Hz) radiations imaged by SEBP.** The circles denote the HF radiators color-coded by rupture time with their sizes proportional to the normalized BP power. The red stars denote the National Earthquake Information Center (NEIC) epicenters for each of the seven supershear earthquakes. The transparent circles of the 2016 Romanche earthquake highlight the back-propagation (southeast-eastward) rupture. The substantial contrast of the color palette near 30 sec is to emphasize the rupture evolutions of shorter and smaller earthquakes like the 2010 M7.0 Papua earthquake.

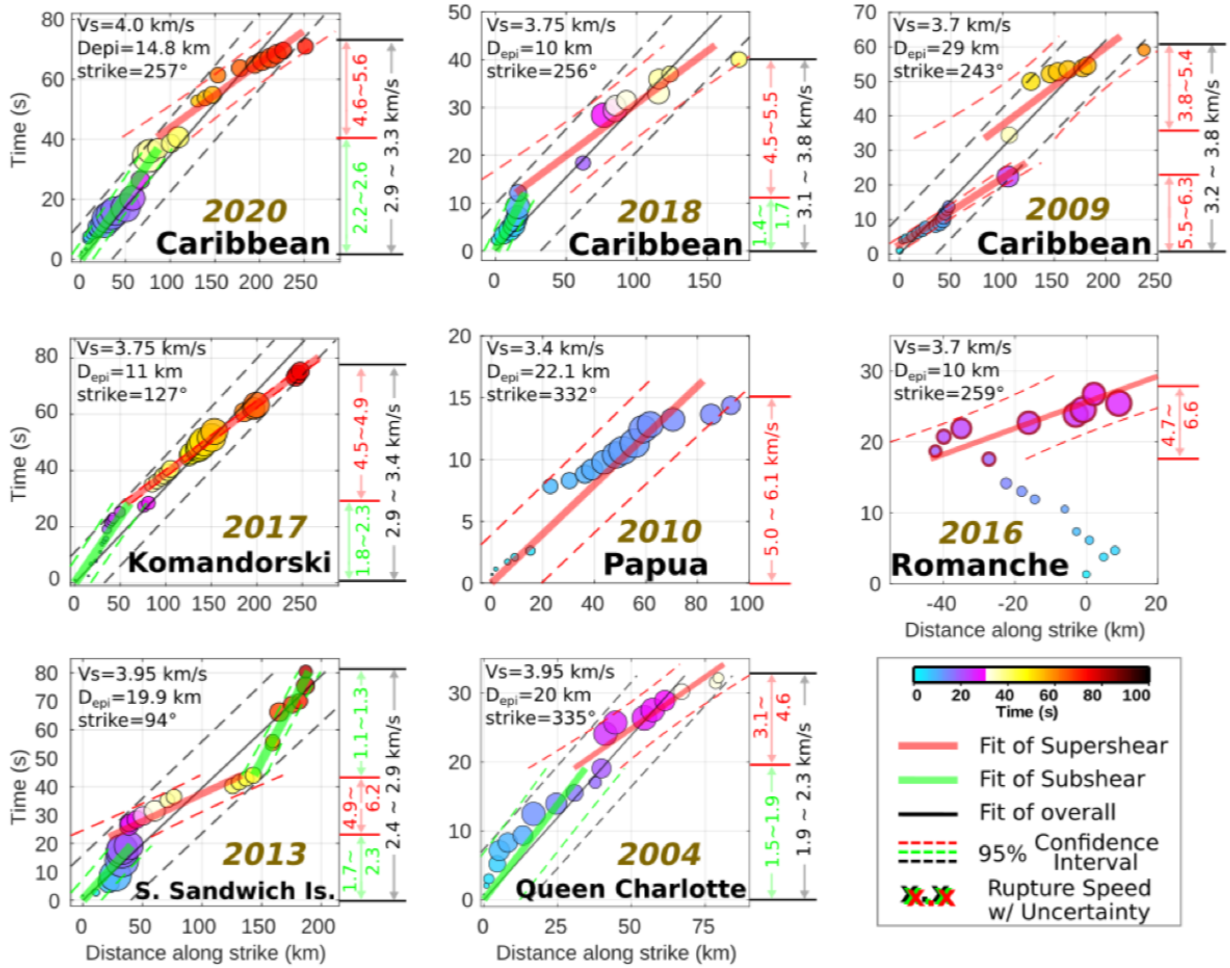

Figure 3. **Estimated rupture speeds of the supershear earthquakes.** The along-strike distances (relative to the hypocenter) of the leading HF radiators imaged by SEBP are plotted against the rupture times (with respect to the origin time). Black (red/green) solid lines and dashed lines are overall (supershear/subshear) rupture speeds and uncertainties estimated based on linear regressions of the radiators, respectively. Through synthetic tests, we found that tracking the leading BP radiators avoids the "shadowing" and "tailing" artifacts that distort the rupture speed estimates (Fig. S15). We also found that the estimated rupture speed is consistently underestimated by 5% ~ 15% (Fig. S17). Therefore, the rupture speed inferred from SEBP is a conservative indicator of supershear ruptures.

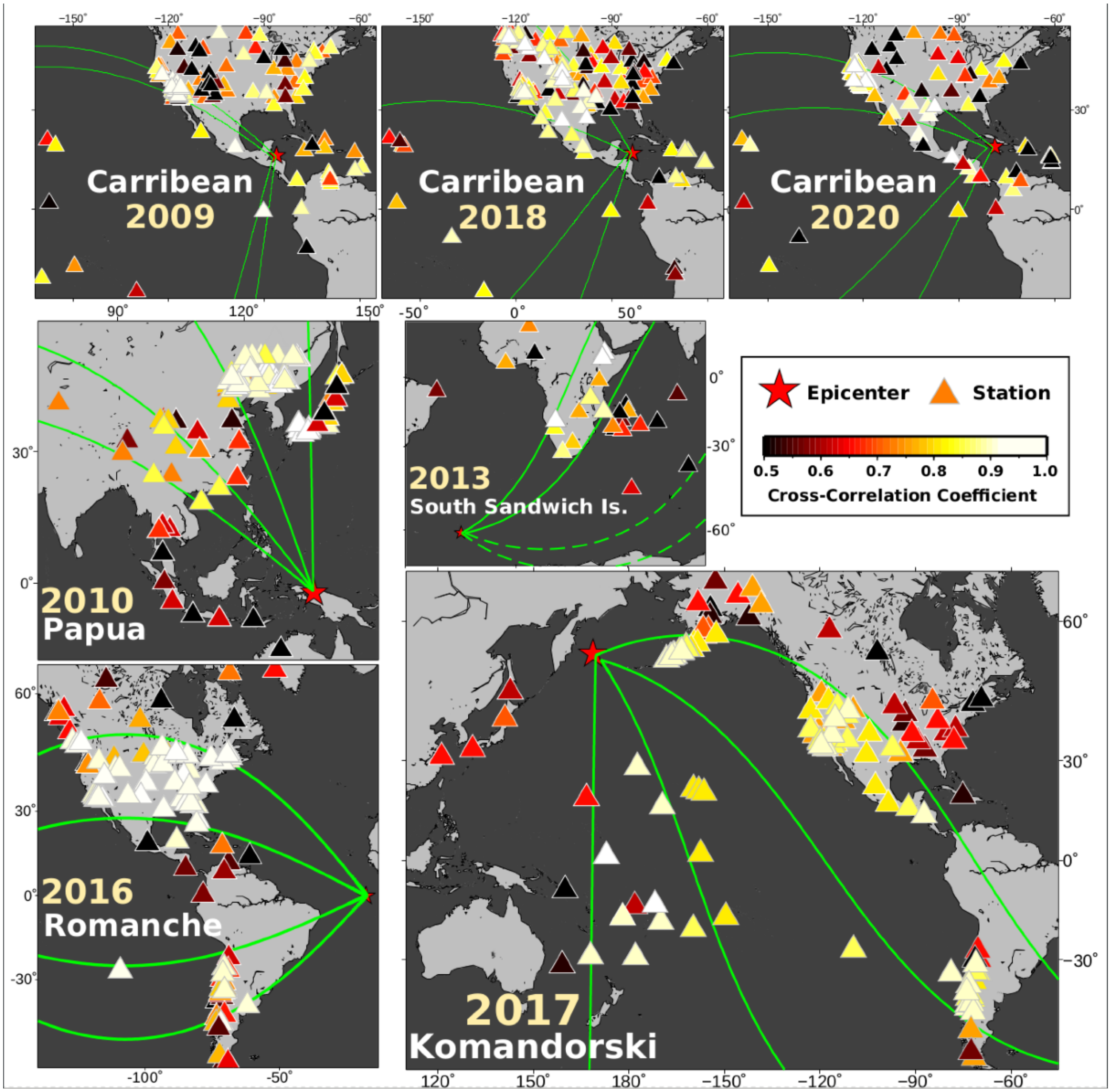

Figure 4. **Evidence of far-field Rayleigh-wave Mach cones.** The area within any two closed green lines is the maximum area predicted by all possible Mach angles, based on the observed rupture speed and the lateral variation of the Rayleigh wave phase velocity (Table S14). The locations of the broadband stations are denoted by triangles. Their color indicates the correlation coefficients of Rayleigh-wave displacement seismograms of the supershear earthquakes and their EGF events (Table S14). The waveform comparisons are shown in Fig. S26.1 to S26.7. The dashed green lines in the figure of the 2013 South Sandwich Island event denote the right-hand side of the predicted Mach cone without any data coverage.

References and Notes

1. Burridge, R. (1973). Admissible speeds for plane-strain self-similar shear cracks with friction but lacking cohesion. *Geophysical Journal International*, *35*(4), 439-455.
2. Andrews, D. J. (1976). Rupture velocity of plane strain shear cracks. *Journal of Geophysical Research*, *81*(32), 5679-5687.
3. Bouchon, M., & Vallée, M. (2003). Observation of long supershear rupture during the magnitude 8.1 Kunlunshan earthquake. *Science*, *301*(5634), 824-826.
4. Bao, H., Ampuero, J. P., Meng, L., Fielding, E. J., Liang, C., Milliner, C. W., ... & Huang, H. (2019). Early and persistent supershear rupture of the 2018 magnitude 7.5 Palu earthquake. *Nature Geoscience*, *12*(3), 200-205.
5. Zhan, Z., Helmberger, D. V., Kanamori, H., & Shearer, P. M. (2014). Supershear rupture in a Mw 6.7 aftershock of the 2013 Sea of Okhotsk earthquake. *Science*, *345*(6193), 204-207.
6. Dunham, E. M., & Bhat, H. S. (2008). Attenuation of radiated ground motion and stresses from three-dimensional supershear ruptures. Journal of Geophysical Research: Solid Earth, 113(B8).
7. Bernard, P., & Baumont, D. (2005). Shear Mach wave characterization for kinematic fault rupture models with constant supershear rupture velocity. Geophysical Journal International, 162(2), 431-447.
8. Bizzarri, A., Dunham, E. M., & Spudich, P. (2010). Coherence of Mach fronts during heterogeneous supershear earthquake rupture propagation: Simulations and comparison with observations. Journal of Geophysical Research: Solid Earth, 115(B8).
9. Vyas, J. C., Mai, P. M., Galis, M., Dunham, E. M., & Imperatori, W. (2018). Mach wave properties in the presence of source and medium heterogeneity. Geophysical Journal International, 214(3), 2035-2052.
10. Das, S. (2015). Supershear Earthquake Ruptures–Theory, Methods, Laboratory Experiments and Fault Superhighways: An Update. In *Perspectives on European Earthquake Engineering and Seismology* (pp. 1-20). Springer, Cham.
11. Passelègue, F. X., Schubnel, A., Nielsen, S., Bhat, H. S., & Madariaga, R. (2013). From sub-Rayleigh to supershear ruptures during stick-slip experiments on crustal rocks. *Science*, *340*(6137), 1208-1211.
12. Bouchon, M., Karabulut, H., Bouin, M. P., Schmittbuhl, J., Vallée, M., Archuleta, R., ... & Marsan, D. (2010). Faulting characteristics of supershear earthquakes. *Tectonophysics*, *493*(3-4), 244-253.
13. Ben-Menahem, A., & Toksöz, M. N. (1963). Source mechanism from spectrums of long-period surface waves: 2. The Kamchatka earthquake of November 4, 1952. *Journal of Geophysical Research*, *68*(18), 5207-5222.
14. Kikuchi, M., & Kanamori, H. (1991). Inversion of complex body waves—III. *Bulletin of the Seismological Society of America*, *81*(6), 2335-2350.
15. Beresnev, I. A. (2003). Uncertainties in finite-fault slip inversions: to what extent to believe?(a critical review). *Bulletin of the Seismological Society of America, 93*(6), 2445-2458.
16. Okuwaki, R., Hirano, S., Yagi, Y., & Shimizu, K. (2020). Inchworm-like source evolution through a geometrically complex fault fueled persistent supershear rupture during the 2018 Palu Indonesia earthquake. *Earth and Planetary Science Letters, 547*, 116449.
17. Spudich, P., & Cranswick, E. (1984). Direct observation of rupture propagation during the 1979 Imperial Valley earthquake using a short baseline accelerometer array. *Bulletin of the Seismological Society of America*, *74*(6), 2083-2114.
18. Bouchon, A., Facchetti, F., Weigand, M. A., & Colonna, M. (2001). TREM-1 amplifies inflammation and is a crucial mediator of septic shock. *nature*, *410*(6832), 1103-1107.
19. Wang, D., & Mori, J. (2012). The 2010 Qinghai, China, earthquake: A moderate earthquake with supershear rupture. *Bulletin of the Seismological Society of America*, *102*(1), 301-308.
20. Ishii, M., Shearer, P. M., Houston, H., & Vidale, J. E. (2005). Extent, duration and speed of the 2004 Sumatra–Andaman earthquake imaged by the Hi-Net array. *Nature*, *435*(7044), 933-936.

21. Meng, L., Zhang, A., & Yagi, Y. (2016). Improving back projection imaging with a novel physics-based aftershock calibration approach: A case study of the 2015 Gorkha earthquake. *Geophysical Research Letters*, *43*(2), 628-636.
22. Pesicek, J. D., Thurber, C. H., Zhang, H., DeShon, H. R., Engdahl, E. R., & Widiyantoro, S. (2010). Teleseismic double-difference relocation of earthquakes along the Sumatra-Andaman subduction zone using a 3-D model. *Journal of Geophysical Research: Solid Earth*, *115*(B10).
23. Vallée, M., & Dunham, E. M. (2012). Observation of far-field Mach waves generated by the 2001 Kokoxili supershear earthquake. *Geophysical Research Letters*, *39*(5).
24. Hicks, S. P., Okuwaki, R., Steinberg, A., Rychert, C. A., Harmon, N., Abercrombie, R. E., ... & Sudhaus, H. (2020). Back-propagating supershear rupture in the 2016 M w 7.1 Romanche transform fault earthquake. *Nature Geoscience*, *13*(9), 647-653.
25. Kehoe, H. L., & Kiser, E. D. (2020). Evidence of a supershear transition across a fault stepover. *Geophysical Research Letters*, *47*(10), e2020GL087400.
26. Tadapansawut, T., Okuwaki, R., Yagi, Y., & Yamashita, S. (2020). Rupture Process of the 2020 Caribbean Earthquake along the Oriente Transform Fault, Involving Supershear Rupture and Geometric Complexity of Fault. *Geophysical Research Letters*, e2020GL090899.
27. DeMets, C., Gordon, R. G., & Argus, D. F. (2010). Geologically current plate motions. *Geophysical Journal International*, *181*(1), 1-80.
28. Graham, S. E., DeMets, C., DeShon, H. R., Rogers, R., Maradiaga, M. R., Strauch, W., ... & Hernandez, D. (2012). GPS and seismic constraints on the M= 7.3 2009 Swan Islands earthquake: implications for stress changes along the Motagua fault and other nearby faults. *Geophysical Journal International*, *190*(3), 1625-1639.
29. Dunham, E. M., & Archuleta, R. J. (2005). Near-source ground motion from steady state dynamic rupture pulses. *Geophysical Research Letters*, *32*(3).
30. Yue, H., Lay, T., Freymueller, J. T., Ding, K., Rivera, L., Ruppert, N. A., & Koper, K. D. (2013). Supershear rupture of the 5 January 2013 Craig, Alaska (Mw 7.5) earthquake. *Journal of Geophysical Research: Solid Earth,* 118(11), 5903-5919.
31. Hayes, G. P. (2017). The finite, kinematic rupture properties of great-sized earthquakes since 1990. *Earth and Planetary Science Letters*, *468*, 94-100.
32. Kogan, M. G., Frolov, D. I., Vasilenko, N. F., Freymueller, J. T., Steblov, G. M., Ekström, G., ... & Prytkov, A. S. (2017). Plate coupling and strain in the far western Aleutian arc modeled from GPS data. *Geophysical Research Letters*, *44*(7), 3176-3183.
33. Gabriel, A. A., Ampuero, J. P., Dalguer, L. A., & Mai, P. M. (2013). Source properties of dynamic rupture pulses with off-fault plasticity. *Journal of Geophysical Research: Solid Earth*, *118*(8), 4117-4126.
34. Dunham, E. M. (2007). Conditions governing the occurrence of supershear ruptures under slip-weakening friction. *Journal of Geophysical Research: Solid Earth*, *112*(B7).
35. Liu, Y., & Lapusta, N. (2008). Transition of mode II cracks from sub-Rayleigh to intersonic speeds in the presence of favorable heterogeneity. *Journal of the Mechanics and Physics of Solids*, *56*(1), 25-50.
36. Dunham, E. M., Favreau, P., & Carlson, J. M. (2003). A supershear transition mechanism for cracks. *Science*, *299*(5612), 1557-1559.
37. Bruhat, L., Fang, Z., & Dunham, E. M. (2016). Rupture complexity and the supershear transition on rough faults. *Journal of Geophysical Research: Solid Earth*, *121*(1), 210-224.
38. Ryan, K. J., & Oglesby, D. D. (2014). Dynamically modeling fault step overs using various friction laws. *Journal of Geophysical Research: Solid Earth*, *119*(7), 5814-5829.
39. Weng, H., & Ampuero, J. P. (2019). The dynamics of elongated earthquake ruptures. *Journal of Geophysical Research: Solid Earth*, *124*(8), 8584-8610.
40. Kaneko, Y., & Lapusta, N. (2010). Supershear transition due to a free surface in 3-D simulations of spontaneous dynamic rupture on vertical strike-slip faults. *Tectonophysics*, *493*(3-4), 272-284.
41. Huang, Y., Ampuero, J. P., & Helmberger, D. V. (2016). The potential for supershear earthquakes in damaged fault zones–theory and observations. *Earth and Planetary Science Letters*, *433*, 109-115.

42. Weng, H., & Ampuero, J. P. (2020). Continuum of earthquake rupture speeds enabled by oblique slip. *Nature Geoscience*, *13*(12), 817-821.
43. Andrews, D. J., & Ben-Zion, Y. (1997). Wrinkle-like slip pulse on a fault between different materials. *Journal of Geophysical Research: Solid Earth*, *102*(B1), 553-571.
44. Weertman, J. (2002). Subsonic type earthquake dislocation moving at approximately× shear wave velocity on interface between half spaces of slightly different elastic constants. *Geophysical research letters*, *29*(10), 109-1.
45. Shi, Z., & Ben-Zion, Y. (2006). Dynamic rupture on a bimaterial interface governed by slip-weakening friction. *Geophysical Journal International*, *165*(2), 469-484.
46. Shlomai, H., & Fineberg, J. (2016). The structure of slip-pulses and supershear ruptures driving slip in bimaterial friction. *Nature communications*, *7*(1), 1-7.
47. Perrin, C., Manighetti, I., Ampuero, J. P., Cappa, F., & Gaudemer, Y. (2016). Location of largest earthquake slip and fast rupture controlled by along-strike change in fault structural maturity due to fault growth. *Journal of Geophysical Research: Solid Earth*, *121*(5), 3666-3685.
48. Freund, L. B. (1979). The mechanics of dynamic shear crack propagation. *Journal of Geophysical Research: Solid Earth*, *84*(B5), 2199-2209.
49. Lay, T., Ye, L., Bai, Y., Cheung, K. F., Kanamori, H., Freymueller, J., ... & Kogan, M. G. (2017). Rupture along 400 km of the Bering fracture zone in the Komandorsky Islands earthquake (MW 7.8) of 17 July 2017. *Geophysical Research Letters*, *44*(24), 12-161.
50. Oral, E., Weng, H., & Ampuero, J. P. (2020). Does a Damaged-Fault Zone Mitigate the Near-Field Impact of Supershear Earthquakes?—Application to the 2018 7.5 Palu, Indonesia, Earthquake. *Geophysical Research Letters*, *47*(1), e2019GL085649.

CORRESPONDING AUTHOR:

Lingsen Meng (Email: meng@epss.ucla.edu)

ACKNOWLEDGEMENTS

We thank J. Fineberg, N. Lapusta, P. Bird, E. Dunham, R. Okuwaki, H. Kehoe, T. Lay, S. Park, and three anonymous reviewers for valuable comments and discussions. We thank H. Weng for the discussion of the effect of energy ratio on rupture sustainability. We thank B. Wu for the discussion of the BP synthetic test. We thank H. Zhang, L. Gao and H. Guo for providing the teleseismic double-difference code.

Funding: Provide complete funding information, including grant numbers, complete funding agency names, and recipient's initials. Each funding source should be listed in a separate paragraph.

NSF grant no. EAR-1848486

Leon and Joanne V.C. Knopoff Foundation

UCAJEDI Investments in the Future project (ANR-15-IDEX-01) managed by the French National Research Agency (ANR)

Author contributions: Each author's contribution(s) to the paper should be listed [we encourage you to follow the CRediT model]. Each CRediT role should have its own line, and there should not be any punctuation in the initials.

Conceptualization: HB, LM, JPA

Methodology: HB

Investigation: HB, LX

Visualization: HB

Funding acquisition: LM, JPA

Supervision: LM

Writing – original draft: HB

Writing – review & editing: HB, LM, JPA

Competing interests: Authors declare that they have no competing interests.

Data and materials availability: All input data (seismograms and travel times) are all available online: the seismic data are provided by the Incorporated Research Institutions for Seismology (IRIS, www.iris.edu) and Observatories & Research Facilities for European Seismology (ORFEUS, www.orfeus-eu.org), and the travel times are provided by the EHB catalogue (www.isc.ac.uk/isc-ehb). All code used in this study are available upon request.

Supplementary Materials

Methods

1. Slowness-Enhanced Back-Projection
2. Synthetic tests of Back-projection and rupture speed estimation.
3. Mach Wave Identification
4. Teleseismic Double-difference Relocation

Supplementary Materials

1. General Information
    - Table S1 Summary of Previous Identified Supershear Earthquakes
    - Table S2 Summary of All Examined Events
    - Table S3 Statistics of Supershear Events
    - Table S4 Summary of Moho and LAB Depths of Supershear Earthquakes
    - Table S5 Summary of Supershear Rupture Speeds

2. Slowness-Enhanced Back-Projection (SEBP)
    - Text S1 Array Selection
    - Table S6 Summary of Array Selection
    - Figure S1 Example of weak and strong pP phase
    - Figure S2.1 ~ S2.8 Maps of SEBP Arrays
    - Table S7.1 Summary of Mainshock Hypocenter Location
    - Table S7.2 Summary of BP Parameters
    - Table S8.1 Summary of Slowness Calibrations (Spatial Bias)
    - Table S8.2 ~ S8.9 Slowness Calibration for Individual Event
    - Figure S3.1 ~ S3.8 Slowness Calibration for Individual Events
    - Figure S4 The Figure 3 (in Main Text) with All BP Radiators
    - Figure S5 BP of the 2004 Queen Charlotte Earthquake
    - Figure S6 SEBP of Multi-arrays of the 2018 Caribbean Earthquakes
    - Figure S7 SEBP of Multi-arrays of the 2020 Caribbean Earthquakes
    - Figure S8 SEBP of the Bilateral Rupture of the 2017 Komandorski Earthquake
    - Figure S9 SEBP of the Bilateral Rupture of the 2020 Caribbean Earthquake

3. Synthetic Back-Projection
    - Text S2 Synthetic Back-Projection (SBP)
    - Figure S10 Model setup of the synthetic rupture.
    - Figure S11 SBP of uniform rupture with constant rupture speed.
    - Figure S12 SBPs of uniform rupture with different rupture speeds
    - Figure S13 SBP of uniform rupture with abrupt change in rupture speed
    - Figure S14 SBPs of uniform rupture with abrupt changes in rupture speeds.
    - Figure S15 SBP of rupture with realistic slip distribution and constant rupture speeds.

Methods

1. Slowness-Enhanced Back-Projection

Back-projection (BP) is an observational technique that tracks the growth of earthquake ruptures based on coherent seismic wavefields recorded by dense networks (*51*), for a comprehensive review). The high-frequency (~ 1 Hz) radiations recovered by BPs indicate the movement of the rupture tip and outline the rupture kinematics, such as the rupture dimensions and speeds (20,52,53). We adopt the Multitaper-MUSIC technique enhanced by the "reference window" strategy, which eliminates "swimming" artifacts and resolves closely spaced simultaneous sources, yielding sharper and more robust source images than the conventional beamforming approach (54,55). In standard BPs, the subsequent rupture locations with respect to the hypocenter are determined based on travel-times inferred from 1-D layered Earth model (e.g., IASP91). A set of static corrections, referred to as "hypocenter correction", estimated by cross-correlating the initial window of P arrivals, are often applied to reduce the travel time errors due to 3-D velocity structures. However, such corrections are valid only in the immediate proximity of the hypocenter. To cover the entire source region, we apply the slowness-enhanced back-projection (SEBP) that accounts for the spatial derivatives of the travel times based on the nearby events (M 4 - 6). For a set of nearby events, their differential travel-times relative to the hypocenter are compared to the predictions of the 1-D Earth model. Then the remaining differences of travel-times are mapped into the slowness corrections. Case studies of the recent large earthquakes (e.g. the 2015 Mw 8.3 Illapel earthquake, the 2017 Mw 8.1 Tehuantepec earthquake, and the 2018 Mw 7.5 Palu earthquake) demonstrate that SEBP provides more accurate source locations and extract more reliable rupture speed estimates. (56,57,4).

We analyzed 57,850 broadband seismograms distributed by the Incorporated Research Institutions for Seismology (IRIS) and Observatories & Research Facilities for European Seismology (ORFEUS). We group the stations into large regional arrays: United States (US), Alaska (AK), pan-Europe (EU), and Australia (AU) (Text S1). For each target event, we perform SEBP to the direct P-wave phases recorded by receiver arrays within epicentral distances between 30° to 90° and without strong depth phases. When multiple arrays are available, we also provide comparisons of SEBP results of different arrays. Text S1, Table S6, and Figure S2 provide details of the array selection and locations. Processing parameters like hypocenter locations, frequency bands and window lengths are provided in Table S7. We derive the slowness correction terms based on 3 to 9 nearby events for each mainshock. These nearby events are evenly distributed across the mainshock rupture path with magnitudes ranging from 4.4 to 6.3 (Table S8). Accurate locations of nearby events are important for reliable slowness calibrations, yet uncertainties of catalog locations can be as large as ~10 km. Therefore, we performed double-difference relocations to obtain higher accuracies of the nearby events' locations that are used for calibration (see Section 3 of Method). After relocation, the relative location uncertainty is decreased to 1~5 km based on Bootstrap analysis (Table S13 & Figure S24), a much smaller discrepancy compared to the root-mean-square (RMS) errors of BP locations of 21 km, defined as the difference between the catalog and the BP-imaged locations of nearby events. Figure S3 compares the BP-imaged locations of nearby events with and without the slowness correction. In all cases, the initial BP locations show systematic biases. Our slowness calibration reduces the RMS errors (between the BP and catalog locations) from 21.2 km to 10.1 km (Table S8). Our confidence in the SEBP comes from the significant reduction of the spatial bias and the better agreement of the BP source locations with traces of fracture zones in the bathymetry (Fig. S3). The rupture speed and uncertainty is estimated in a conservative yet robust way under the guidance of a comprehensive series of synthetic tests of BP (see Method Section 4).

2. Synthetic tests of Back-projection and rupture speed estimation.

To understand potential artifacts of our BP results and to guide the estimation of the rupture speeds, we conduct comprehensive synthetic tests of BP considering (1) different scenarios of rupture kinematics (different rupture speeds, segmentations with rupture speeds changes, e.g., supershear transition from subshear speeds to supershear speeds), (2) realistic slip distribution constrained by various finite source models, and most importantly, (3) realistic waveform complexities, which is one of the main causes of BP artifacts and uncertainties. Here, we provide a short summary of the methodology, modeling setup and data, results, and how the results are used to guide estimations of rupture speeds and uncertainties, while Text S2 provides a thorough description with much more details.

Recently, many studies of synthetic BP have shed light on connecting BP images with fault kinematics. However, two critical problems prohibit general applications of the results of these studies: (1) multiple point source models with large spatial and temporal separation do not properly represent waveform interference of neighboring sub-sources (54,58,59); (2) deterministic Green's functions calculated assuming either a homogeneous full space (60) or a 1D layered Earth model (61,62) do not include heterogeneity-induced scattered and coda waves and thus fail to reproduce the realistic waveform complexities that are a key cause of BP artifacts. To address these two problems, we take into account nine slip models of previous strike-slip events, apply dense discretization, and apply an interpolation/extrapolation method to generate Green's functions from several empirical Green's function events (EGFs). Such a setup introduces the keys to realistic synthetics: interference between waveforms from sub-sources and coherence fluctuations of array recordings. We assume the earthquake source region has similar random features as the crust and upper mantle and alternate the Green's function of assumed EGF events along the strike at a similar correlation length of 20 km (64). We normalize all EGFs P wave amplitudes at the frequency 0.5 ~ 2 Hz to mitigate any potential finite source effects.

We set our synthetic rupture at the source region of the 2020 Caribbean earthquake and assume the same hypocenter (19.419°N 78.756°W, NEIC) and same strike angle (255°) with a westward propagation (Fig. S10). The fault surface dimension is set to be 300 km long and 15 km wide and discretized into elements with size [200 m x 200 m]. Considering the limited signal-noise-ratio (SNR) of small earthquakes at teleseismic distance, the best candidates are three M 5 ~ 6 events (Fig. S10). The synthetic waveforms are calculated as the sum of slip-rate contributions from each element convolved with empirical Green's functions (EGFs) (Text S2). The Yoffe analytical function (65,66) is chosen as the slip-rate function (see Text S2 for details). A short summary of the results of the synthetic test are provided below, while detailed results are described in Text S2, Figures S10 ~ S17.

We find that two styles of artifacts, the shadowing and tailing artifacts can distort the rupture speed estimation (Figures S13 & S15). The shadowing artifacts refers to BP radiators with significant power that are followed by a group of stagnant or back-propagating radiators, even though the actual (input) rupture is still moving forward. We found that shadowing artifacts can be caused by abrupt changes in rupture speeds (e.g., supershear transitions) or abrupt changes in slip distribution along the fault surface (Figures S13 & S15). Such an artifact tends to mask the continuous rupture and contaminates BP results. The tailing artifact refers to the additional radiators in BP even after the rupture stops, which often show apparent back-propagation.

To counter the effects of these artifacts, we take the following strategy. First, we found that keeping the leading BP radiators removes the tailing artifact completely and most of the shadowing artifact. If an earthquake does not show significant rupture speed change, we fit the overall rupture speed based on the leading radiators. Earthquakes that meet this condition are 2010 Papua earthquakes. However, many ruptures show stages of different rupture speeds. For example, supershear earthquakes often start with a slow initiation in the beginning and then transit into a faster stage. If the location of a rupture speed change does not involve a corresponding shadowing artifact, we fit the leading radiators since the velocity changes. Earthquakes that meet this condition are the 2017 Komandorski and 2016 Romanche earthquakes. For earthquakes involving strong shadowing artifacts, we exclude the contaminated radiators of shadowing artifacts in the rupture speed fitting. Our synthetic tests show the shadowing artifacts are often associated with a local temporal maximum of BP power followed by stagnation or reverse-propagation of BP radiators

(Figures S14). In practice, we divide the earthquake into separated stages before and after the shadowing artifacts and estimate the rupture speeds based on the leading radiators of each stage. Earthquakes that meet this condition are the 2018 Caribbean, 2020 Caribbean, 2013 South Sandwich Island, 2009 Caribbean, and 2004 Queen Charlotte earthquakes.

We further found that the fitted rupture speeds (V_{fit}) are systematically underestimated due to the averaging effect of direct and coda waves (Figure S17, S19, & S20). This hypothesis is supported by synthetic tests using EGF without coda waves, which shows that the V_{fit} is no longer systematically smaller than the input rupture speed (V_r). Then, by comparing V_{fit} and V_r over a range of V_r, we find that V_r can be written as:

$$V_r = 1.21\, V_{fit} - 0.37$$

This means for V_{fit} = 3 km/s, V_r = 3.26 kms (8% underestimation), for V_{fit} = 4km/s, V_r= 4.47 km/s (11% underestimation), and for V_{fit} = 5 km/s, V_r = 5.68 km/s (12% underestimation). The complete expression considering confidence intervals of linear fitting errors can be found in Figure S17. More details can be found in Text S3 and Table S12.

We note that fault geometry can be an extra source of uncertainty because how the fault geometry is determined can affect the rupture speed estimation of BP. For example, one can define the rupture direction using focal mechanism solutions like USGS or GCMT, or by linearly best-fitting the BP radiators, or based on fault traces as indicated from topography, field survey and geodetic measurements. Table S9 shows how these different approaches to determine a fault geometry influences the rupture speed estimation. We found that the resulting rupture speed uncertainties of all the investigated supershear earthquakes is between 0.5% to 3.0%, much smaller than the uncertainty due to averaging effect of direct and coda waves mentioned above. On the other hand, our synthetic tests show that the window length and frequency band of BP can influence the rupture speed estimation/uncertainty (Figure S22, Figure S23, Table S10, and Table S11). We found that (1) there is a trade-off between temporal resolution (shorter windows give higher temporal resolutions) and robustness of rupture speed estimation (longer windows correspond to smaller uncertainties); (2) there is another trade-off between spatial resolution (higher frequency bands give higher spatial resolutions) and robustness of rupture speed estimation (lower frequency band gives more stable fitting). To balance the spatial and temporal resolution and robustness of rupture speed fitting, we prefer a window length of 10 sec and a frequency band of 0.5-2 Hz for our uncertainty analysis.

3. Mach Wave Identification

Mach waves, a unique signature of supershear ruptures, can be effectively identified in the far-field surface wavefield. For earthquakes rupturing at velocities slower than Rayleigh wave speed, wavefronts from different sub-sources arrive at any far-field receiver at different times. For supershear earthquakes, only at stations located on the Rayleigh Mach cone do waves from different parts of a supershear rupture arrive simultaneously and interfere constructively, resulting in an apparent point-source. As first proposed by Vallée and Dunham (23), along the Mach cone, the waveform of a supershear mainshock should be identical to that of a smaller reference event, referred to as an empirical Green's function (EGF) event, with a similar focal mechanism in the vicinity of the mainshock. The Mach wave identification is conducted by evaluating the waveform similarity between a target event and its collocated EGF. We use the standard cross-correlation CC to estimate the waveform similarity. $CC(U,u) = \sum_{i=1}^{N} U_i u_i / \sqrt{\sum_{i=1}^{N} U_i U_i \sum_{i=1}^{N} u_i u_i}$, where U and u are the discrete time-series of the mainshock and the EGF event, respectively.

To maintain the finite-source effect of the mainshock and the point-source effect of the EGF, the waveforms should be compared at periods shorter than the duration of the mainshock T0 and longer than the duration of the EGF TEGF. Given that T_0= 24 ~ 50 s and T_{EGF}= 0.8 ~ 9 s (Table S14), we use a 15-25 s bandpass filter for the Mw 7.3 ~ 7.7 events and 10-20 s filter for Mw 7.0 ~ 7.1 events. Considering the travel-time errors due to surface wave dispersion and 3D path effect, we manually identify the EGF Rayleigh-wave arrivals, which are simpler and more straightforward to pick than those of the mainshocks. For each station, we choose 200 ~ 400 s long cross-correlation windows to include the entire envelope of the EGF wave trains (due to dispersion, the envelope becomes longer at larger hypocenter distances) (Fig. S25 & Fig. S26). We assume the same arrival times and use the same windowing for the mainshock Rayleigh waves. Since supershear rupture rarely starts from the beginning of the earthquake, we allow lag times up to the half duration of the mainshock when calculating CC. The Python software package Obspy (67) was used for data requesting, waveform filtering and cross-correlation processing.

The source directivity effect relates the observed high waveform similarities to the locations of the Mach cones. The apparent source duration T_a of the mainshock is equal to the true duration T_0 scaled by the directivity factor: $T_a = T_0 \times D(\Phi)$. $D(\Phi) = 1 - cos(\Phi)V_r/V_{Rayleigh}$ where Φ is the receiver azimuth relative to the rupture direction, Vr is the rupture speed, and $V_{Rayleigh}$ is the Rayleigh wave speed at the center period T_c of the waveform filter. Given the short duration of the EGF event, the mainshock waveform is similar to that of the EGF if the mainshock also appears as an apparent point source, which requires $T_a \ll T_c$. If T_c~ 20 s and T_0 ~ 40 s, the two events are of high similarity when $|D(\Phi)| \ll$ 0.5. This condition is met near and on the Mach cone where the $D(\Phi)$ is minimized. The pattern of the D factor as a function of receiver azimuth is shown in Fig. S29. We have also constructed synthetic rupture scenarios with various rupture speeds and compared their waveform similarities with the EGF (Text S4). For fast sub-Rayleigh ruptures, waveform similarity is maximized in the rupture direction, illustrated by Figs. S28 & S29 and the example of the Kumamoto earthquake (Fig. S25). For supershear ruptures, waveform similarity reaches its maximum on the two Mach cones, consistent with the patterns of the 2009 Caribbean, 2018 Caribbean, 2010 Papua, 2016 Romanche, and 2013 South Sandwich Island events (Fig 3, 4, & S25). The waveform similarity can also be relatively high in between the Mach Cones but still lower than that in the Mach cones if the rupture speed is only moderately faster than the S wave (see the pattern of the Directivity Factor and also synthetic test in Fig. S29), as is the case of the 2017 Kormandosky event. No Mach waves are identified for the 2004 Queen Charlotte earthquake, which is likely due to the fact that its supershear propagation distance (~ 40 km) is not sufficiently long compared to its seismogenic width (23).

The amplitude information can also be used to identify the supershear event, since the amplitude ratio between the Rayleigh Mach wave of the supershear earthquake and that of the EGF event should equal their moment ratio:

$$\frac{std(U)}{std(u)} = \frac{M_0}{M_{EGF}}$$

where std is the standard deviation of surface waves, and M_0 and M_{EGF} are the moment of the mainshock and EGF event, respectively. However, since most of the supershear earthquakes do not propagate at supershear rupture speeds entirely, the moment of a supershear rupture is only a part of M_0. Therefore, the waveform amplitude ratio $std(U)/std(u)$ tends to be smaller than the moment ratio M_0/M_{EGF}. However, the azimuthal pattern of the amplitude-ratio (AR) can still distinguish sub-Rayleigh and supershear events.

$$AR = \frac{std(U)/M_0}{std(u)/M_{EGF}}$$

Fig. S29 demonstrates AR as a function of azimuth based on synthetic tests of elongated ruptures with different rupture speeds. We find that for sub-Rayleigh ruptures, the distribution is unimodal with the highest amplitude ratio in the rupture direction, while that of supershear rupture is bimodal with high amplitude ratios on each of the Mach cones (Fig. S29). These patterns are consistent with the distributions of our newly identified supershear events (the 2009 Caribbean, 2010 Papua, 2013 South Sandwich Island, 2016 Romanche, 2017 Komandorski, 2018 Caribbean, 2020 Caribbean) (Fig. S25). Particularly, for the 2017 Komandorski event with moderately fast rupture speed, the amplitude ratios show larger contrast between the Mach cones and the front direction than that of the waveform similarities, and can therefore provide further validation of its supershear speed.

4. Teleseismic Double-difference Relocation

Accurate locations of the events used for the calibration of SEBP are crucial. Therefore, we performed double-difference (DD) relocations to obtain higher accuracy of the nearby events used for calibration. The traditional DD method (68) requires a dense local seismometer network, which is seldom the case for the oceanic earthquakes analyzed in this study. However, Pesicek et al. (22) designed a teleseismic DD relocation method and applied it to analyze both the seismicity and the velocity structure in the Andaman-Sumatran region. Here, we use the same method with the initial velocity model fixed and only use the relocation function. In teletomoDD, travel-time calculations are performed using pseudo-bending raytracing (69) adapted for usage in a spherical coordinate system by Koketsu and Sekine (70). This raytracing method allows usage of local, regional, and teleseismic P- and S-wave arrival-time data. Therefore, errors due to the insufficient number of data and azimuthal gaps in the seismic network based on local data can be minimized.

We relocate earthquakes in each of the mainshock regions by combining arrival-time data of P and S waves from local, regional, and teleseismic stations in the periods of 2000 to 2020. The catalog data and arrival time data were taken from the Engdahl–van der Hilst–Buland (EHB, http://www.isc.ac.uk/ehbbulletin/search/catalogue/) for the period of 2000 to 2016 and from the USGS ANSS Comprehensive Earthquake Catalog (ComCat, https://earthquake.usgs.gov/data/comcat/) for the time period of 2017-2020. A Python package, libcomcat (https://github.com/usgs/libcomcat), is used to retrieve the ComCat data. To form the catalog differential times, we followed Waldhauser and Schaff (71) and Pesicek et al. (22) and linked each event with its 20 nearest neighbors within 300 km that had at least 15 commonly observed phases at stations within 90°, requiring a minimum of 10 differential time links per pair. We limited the earthquake data to those locations with an azimuthal gap of less than 210° (72). The travel times were calculated using a 3D global velocity model with a grid size of 1°× 1°, TX2019slab (73). We also performed a similar hierarchical dynamic weighting scheme as Waldhauser and Ellsworth (68), Zhang and Thurber (74), Waldhauser and Schaff (71), and Pesicek et al. (22) to properly account for the varying data quantities, types, and qualities. In this scheme, the weighting of absolute data was initially high and gradually lowered during subsequent iteration, while the weighting of differential times was initially low but progressively increased. Such type of weighting allows for initial improvements to the absolute locations using the 3-D velocity model and determination of more precise relative locations due to the use of differential times.

Our relocation results show improvements in the spatial distribution of seismicity around the fault zones. Figure S24 shows the comparison of events locations before and after relocations. All of the relocated hypocenter distributions show more clustered patterns compared to those based on the EHB and USGS catalog. Significant reductions in travel-time residuals range from 50% to 78%. For each relocation, the number of stations, number of data, reduction of travel-time residuals, and mean values of location shifts are summarized in Table S13. Files of the relocated catalogs can be found in supplementary materials.

To evaluate the absolute location uncertainty and the relative location uncertainty, we performed Jackknife and Bootstrap analysis. The Jackknife analysis estimates the absolute location uncertainties by recomputing the locations a hundred times using different subsets of recording stations, each with 10% of the stations removed. The Bootstrap analysis estimates the relative location uncertainties by recomputing the locations a hundred times after adding random Gaussian noise to the travel times with a standard deviation of 0.5 s. Figure S24 shows the result of the Jackknife and Bootstrap analyses. After relocation, the relative location uncertainties drop to 1 ~ 3 km, which is more than sufficient for SEBP calibration. A summary of the location uncertainties can be found in Table S13.

References and Notes

51. Kiser, E., & Ishii, M. (2017). Back-projection imaging of earthquakes. *Annual Review of Earth and Planetary Sciences, 45*, 271-299.
52. Kiser, E., & Ishii, M. (2011). The 2010 Mw 8.8 Chile earthquake: Triggering on multiple segments and frequency-dependent rupture behavior. *Geophysical Research Letters*, 38(7).
53. Yao, H., Shearer, P. M., & Gerstoft, P. (2013). Compressive sensing of frequency-dependent seismic radiation from subduction zone megathrust ruptures. *Proceedings of the National Academy of Sciences, 110*(12), 4512-4517.
54. Meng, L., Inbal, A., & Ampuero, J. P. (2011). A window into the complexity of the dynamic rupture of the 2011 Mw 9 Tohoku-Oki earthquake. *Geophysical Research Letters, 38*(7).
55. Meng, L., Ampuero, J. P., Luo, Y., Wu, W., & Ni, S. (2012). Mitigating artifacts in back-projection source imaging with implications for frequency-dependent properties of the Tohoku-Oki earthquake. *Earth, planets and space, 64*(12), 1101-1109.
56. Meng, L., Bao, H., Huang, H., Zhang, A., Bloore, A., & Liu, Z. (2018). Double pincer movement: Encircling rupture splitting during the 2015 Mw 8.3 Illapel earthquake. *Earth and Planetary Science Letters, 495*, 164-173.
57. Meng, L., Huang, H., Xie, Y., Bao, H., & Dominguez, L. A. (2019). Nucleation and kinematic rupture of the 2017 Mw 8.2 Tehuantepec earthquake. *Geophysical Research Letters, 46*(7), 3745-3754.
58. Yao, H., Gerstoft, P., Shearer, P. M., & Mecklenbräuker, C. (2011). Compressive sensing of the Tohoku-Oki Mw 9.0 earthquake: Frequency-dependent rupture modes. *Geophysical Research Letters, 38*(20).
59. Wang, D., Mori, J., & Koketsu, K. (2016). Fast rupture propagation for large strike-slip earthquakes. *Earth and Planetary Science Letters, 440*, 115-126.
60. Yin, J., & Denolle, M. A. (2019). Relating teleseismic backprojection images to earthquake kinematics. Geophysical Journal International, 217(2), 729-747.
61. Koper, K. D., Hutko, A. R., Lay, T., & Sufri, O. (2012). Imaging short-period seismic radiation from the 27 February 2010 Chile (Mw 8.8) earthquake by back-projection of P, PP, and PKIKP waves. *Journal of Geophysical Research: Solid Earth, 117*(B2)
62. Okuwaki, R., Kasahara, A., Yagi, Y., Hirano, S., & Fukahata, Y. (2019). Backprojection to image slip. *Geophysical Journal International, 216*(3), 1529-1537.
63. Berteussen, K. A., Magnus, I., & Edvardsen, A. (1988). 3-D positioning of offset VSP data. In SEG Technical Program Expanded Abstracts 1988 (pp. 823-826). Society of Exploration Geophysicists.
64. Capon, J., & Berteussen, K. A. (1974). A random medium analysis of crust and upper mantle structure under NORSAR. *Geophysical Research Letters, 1*(7), 327-328.
65. Yoffe, E. H. (1951). LXXV. The moving griffith crack. *The London, Edinburgh, and Dublin Philosophical Magazine and Journal of Science, 42*(330), 739-750.
66. Tinti, E., Fukuyama, E., Piatanesi, A., & Cocco, M. (2005). A kinematic source-time function compatible with earthquake dynamics. *Bulletin of the Seismological Society of America, 95*(4), 1211-1223.
67. Krischer, L., Megies, T., Barsch, R., Beyreuther, M., Lecocq, T., Caudron, C., & Wassermann, J. (2015). ObsPy: A bridge for seismology into the scientific Python ecosystem. Computational Science & Discovery, 8(1), 014003.
68. Waldhauser, F., & Ellsworth, W. L. (2000). A double-difference earthquake location algorithm: Method and application to the northern Hayward fault, California. *Bulletin of the seismological society of America, 9*0(6), 1353-1368.

69. Um, J., & Thurber, C. (1987). A fast algorithm for two-point seismic ray tracing. *Bulletin of the Seismological Society of America, 77*(3), 972-986.
70. Koketsu, K., & Sekine, S. (1998). Pseudo-bending method for three-dimensional seismic ray tracing in a spherical earth with discontinuities. *Geophysical Journal International, 132*(2), 339-346.
71. Waldhauser, F., & Schaff, D. (2007). Regional and teleseismic double-difference earthquake relocation using waveform cross-correlation and global bulletin data. *Journal of Geophysical Research: Solid Earth, 112*(B12).
72. Bai, L., Wu, Z., Zhang, T., & Kawasaki, I. (2006). The effect of distribution of stations upon location error: Statistical tests based on the double-difference earthquake location algorithm and the bootstrap method. *Earth, Planets and Space, 58*(2), e9-e12.
73. Lu, C., Grand, S. P., Lai, H., & Garnero, E. J. (2019). TX2019slab: A new P and S tomography model incorporating subducting slabs. *Journal of Geophysical Research: Solid Earth, 124*(11), 11549-11567.
74. Zhang, H., & Thurber, C. H. (2003). Double-difference tomography: The method and its application to the Hayward fault, California. *Bulletin of the Seismological Society of America, 93*(5), 1875-1889.